nature materials

LETTERS

PUBLISHED ONLINE: 30 MAY 2016 | DOI: 10.1038/NMAT4654

Mechanosensitive subcellular rheostasis drives emergent single-cell mechanical homeostasis

Shinuo Weng[1†], Yue Shao[1†], Weiqiang Chen[1‡] and Jianping Fu[1,2,3*]

Mechanical homeostasis—a fundamental process by which cells maintain stable states under environmental perturbations—is regulated by two subcellular mechanotransducers: cytoskeleton tension and integrin-mediated focal adhesions (FAs)[1-5]. Here, we show that single-cell mechanical homeostasis is collectively driven by the distinct, graduated dynamics (rheostasis) of subcellular cytoskeleton tension and FAs. Such rheostasis involves a mechanosensitive pattern wherein ground states of cytoskeleton tension and FA determine their distinct reactive paths through either relaxation or reinforcement. Pharmacological perturbations of the cytoskeleton and molecularly modulated integrin catch–slip bonds biased the rheostasis and induced non-homeostasis of FAs, but not of cytoskeleton tension, suggesting a unique sensitivity of FAs in regulating homeostasis. Theoretical modelling revealed myosin-mediated cytoskeleton contractility and catch–slip-bond-like behaviours in FAs and the cytoskeleton as sufficient and necessary mechanisms for quantitatively recapitulating mechanosensitive rheostasis. Our findings highlight the previously underappreciated physical nature of the mechanical homeostasis of cells.

Homeostasis, a critical biological process to stabilize whole-cell/tissue physiology against external perturbations, has been commonly investigated at the cellular level and beyond[6,7]. Yet, it remains elusive as to how homeostasis, as a cell-driven biological property, arises from collective, dynamic subcellular events. Understanding homeostasis down to a subcellular scale can provide unprecedented insights into the origin and regulation of cell homeostatic behaviours, dysregulation of which has been associated with pathophysiological conditions in developmental disorders, cardiovascular and inflammatory diseases, and cancer[8,9].

Recently, mounting evidence has identified mechanical homeostasis as an important component of the overall cell homeostasis[1–5], wherein the actin cytoskeleton (CSK) tension and integrin-mediated focal adhesion (FA) are two central regulators directly interacting with external biophysical stimuli to elicit downstream mechanotransductive signalling and cell homeostatic behaviours to maintain stable mechanobiological states (phenotypes)[10,11] (Fig. 1a). Therefore, we selected CSK tension and FA as subcellular markers and regulators of mechanical homeostasis, and studied how their rapid, mechanosensitive dynamics at a subcellular scale could collectively drive single-cell mechanical homeostasis as an emergent biological phenomenon in response to external biophysical stimulation.

To visualize FA dynamics and quantify CSK tension, rat embryo fibroblasts (REF-52) stably expressing yellow fluorescent protein (YFP)–paxillin fusion proteins were assayed using a stretchable micropost array (SμPA) cytometry to apply defined static equibiaxial cell stretches simulating external mechanical stimulation (Supplementary Fig. 1; Methods). Deflections of microposts underlying cells seeded on the SμPA cytometry were continuously monitored using fluorescence microscopy for quantification of dynamic subcellular CSK tension (Fig. 1b,c and Supplementary Fig. 2a). Clustering of paxillin, a protein residing in FA and involved in FA assembly and disassembly[12], on micropost tops was recorded simultaneously to examine subcellular FA dynamics[4,13–15] (Fig. 1c and Supplementary Fig. 2b–g, and Supplementary Fig. 3). Together with live-cell fluorescence microscopy, the SμPA was capable of applying controlled equibiaxial cell stretches while simultaneously reporting dynamic responses of subcellular CSK tension and corresponding FA size (represented by paxillin fluorescence intensity) with a one-to-one spatial registration.

We first examined whether individual REF-52 fibroblasts would exhibit mechanical homeostasis at a global cellular scale. Before cell stretch, whole-cell summation of CSK tension and FA size of single REF-52 fibroblasts remained constant as mechanobiological ground (quasi-static) states, and they restored their respective ground-state values at the single-cell level within 30 min after the onset of 8% static equibiaxial stretch (Fig. 1d,e and Supplementary Fig. 4). Such homeostatic behaviours of REF-52 fibroblasts at the single-cell level for both CSK tension and FA were characterized by biphasic dynamics comprising an acute excitation phase within 1 min after the onset of stretch (Phase I; $t = 0$–1 min), followed by another decay phase within 1–30 min following stretch (Phase II; $t = 1$–30 min), in which both whole-cell CSK tension and FA decreased monotonically to their respective ground states (Fig. 1d,e and Supplementary Fig. 4).

Detailed subcellular analysis using paired CSK tension–FA size data pooled from single REF-52 fibroblasts revealed strong linear correlation and temporal synchronization between subcellular CSK tension and FA size during the entire mechanical homeostasis of REF-52 fibroblasts when responding to 8% static equibiaxial stretch (Fig. 1f and Supplementary Fig. 5), suggesting interdependence and temporal synchronization of CSK tension and FA morphogenesis as persistent and robust properties associated with homeostasis. Strikingly, at the subcellular level, however, highly heterogeneous, non-homeostatic behaviours were observed for individual FAs and their associated CSK tension (Fig. 1g–i). After initial excitation in Phase I, individual FAs and their dynamically correlated CSK tension could undergo either relaxation or reinforcement in Phase II of the homeostatic response (Fig. 1g–i).

[1]Department of Mechanical Engineering, University of Michigan, Ann Arbor, Michigan 48109, USA. [2]Department of Biomedical Engineering, University of Michigan, Ann Arbor, Michigan 48109, USA. [3]Department of Cell and Developmental Biology, University of Michigan Medical School, Ann Arbor, Michigan 48109, USA. [†]These authors contributed equally to this work. [‡]Present address: Department of Mechanical and Aerospace Engineering, New York University, New York, New York 10012, USA. *e-mail: jpfu@umich.edu

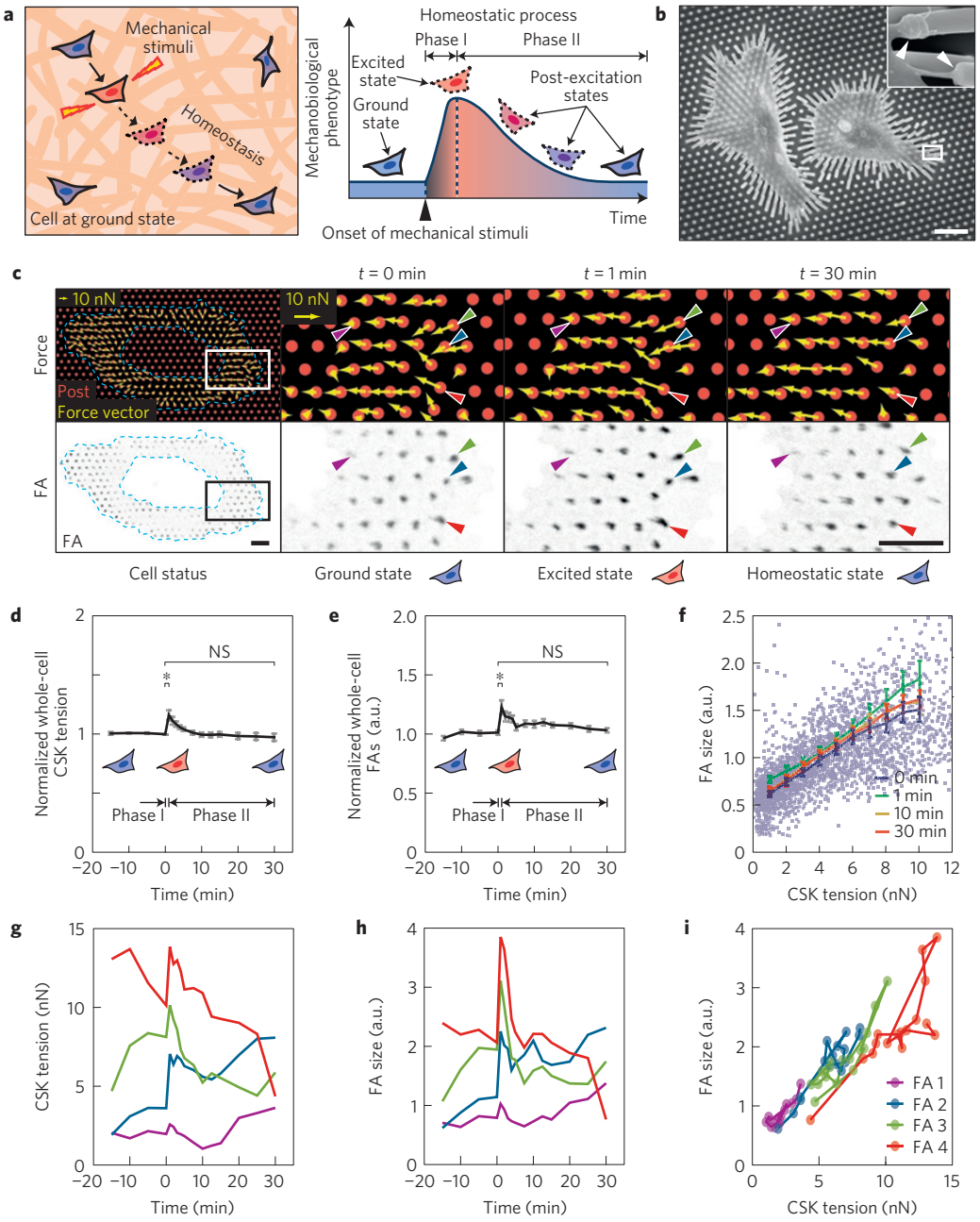

Figure 1 | Dynamics of subcellular cytoskeleton (CSK) tension and focal adhesion (FA) during single-cell mechanical homeostasis. a, Conceptual schematic of single-cell mechanical homeostasis. On mechanical perturbation, a biphasic cellular response comprising an excitation phase (Phase I) followed by another decay phase (Phase II) restores ground states of cellular mechanobiological phenotypes through actively regulated feedback mechanisms. **b**, SEM image showing single REF-52 fibroblasts adhering to micropost tops through individual FAs marked by white arrows in the inset. White rectangle highlights the area in which the inset SEM image was taken. Deflections of microposts due to CSK tension were evident. Scale bar, 20 μm. **c**, Top panel: force vector maps showing subcellular CSK tension (yellow arrows) exerted on micropost tops (red circles) in a single REF-52 fibroblast before ($t = 0$ min, ground state) and after ($t = 1$ min, excited state; $t = 30$ min, homeostatic state) the onset of 8% static equibiaxial stretch. Bottom panel: corresponding fluorescence microscopy images showing individual FAs and their one-to-one spatial registrations to subcellular CSK tension as illustrated by four single FAs marked by colour-coded arrowheads. Region of interest enclosed by blue dashed polygons excluded the nucleus and perinuclear region where FA size and CSK tension were significantly lower compared with other subcellular regions. White (top) and black (bottom) rectangles marked areas where zoom-in images of subcellular CSK tension and FA are shown, respectively. Scale bar, 10 μm. **d**,**e**, Temporal evolutions of normalized whole-cell CSK tension (**d**) and FA size (**e**) during single-cell mechanical homeostasis for REF-52 fibroblasts under 8% static equibiaxial stretch. Data for each single cell were normalized to ground-state values at $t = 0$ min. Data represent the mean ± standard error of the mean (s.e.m.) with $n = 10$. *P*-values were calculated using Student's paired sample *t*-test comparing data before ($t = 0$ min) and after ($t = 1$ min and 30 min) cell stretch. NS, statistically insignificant and $P > 0.05$.*, $P < 0.05$. **f**, Paired subcellular CSK tension–FA size data showing correlation during mechanical homeostasis. Data points represent individual FAs detected at $t = 0$ min. More than 2,500 FAs were analysed from $n = 10$ REF-52 fibroblasts. Data trends are plotted as moving averages (solid lines) ± s.e.m. Mean results obtained at $t = 0$, 1, 10, 30 min are plotted as indicated. **g**,**h**, Temporal evolutions of CSK tension (**g**) and FA size (**h**) for four representative single FAs (marked by colour-coded arrowheads in **c**) during single-cell mechanical homeostasis. **i**, Temporal trajectories of paired CSK tension–FA size data for the same four single FAs in **g**,**h** during single-cell homeostasis.

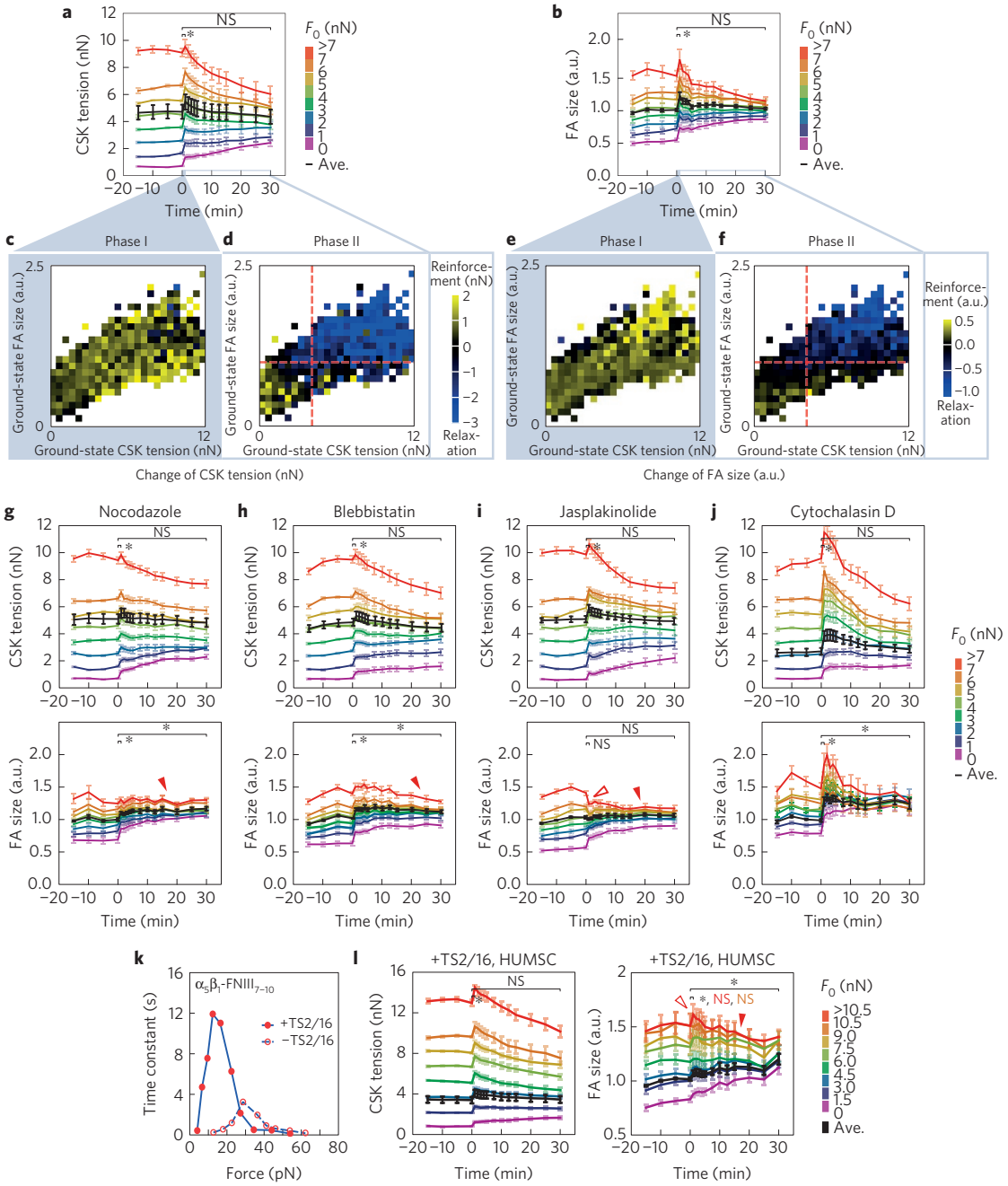

Figure 2 | Subcellular cytoskeleton (CSK) tension and focal adhesion (FA) followed distinct mechanosensitive rheostasis to drive single-cell mechanical homeostasis. a,**b**, Heterogeneous rheostatic paths for subcellular CSK tension (**a**) and FA (**b**). Results from REF-52 fibroblasts under 8% static equibiaxial stretch were grouped into subsets on the basis of ground-state CSK tension values at $t = 0$ min (F_0). Average result from each subset was plotted using the rainbow spectrum (from purple to red). Whole-cell average response (black) was included for referencing single-cell homeostasis. Data represent the mean ± s.e.m. with $n = 10$. **c**–**f**, Dependence of subcellular rheostasis on ground-state values of CSK tension and FA size. Changes in CSK tension (**c**,**d**) and FA size (**e**,**f**) during Phase I ($t = 0$–1 min; **c**,**e**) and phase II ($t = 1$–30 min; **d**,**f**) were colour-coded in two-dimensional ground-state CSK tension–FA size diagrams obtained at $t = 0$ min. Red dashed lines in **d** and **f** marked average ground-state values of CSK tension and FA size as well as a transition boundary between reinforcement and relaxation for subcellular rheostasis during Phase II. **g**–**j**, Responses of subcellular CSK tension (top) and FA (bottom) rheostasis to pharmacological inhibitors in REF-52 fibroblasts under 8% static equibiaxial stretch (**g**: nocodazole; **h**: blebbistatin; **i**: jasplakinolide; **j**: cytochalasin D). Results were grouped into subsets on the basis of ground-state CSK tension values at $t = 0$ min (F_0). Whole-cell average responses (black) were included to indicate changes in single-cell homeostasis. Data represent the mean ± s.e.m. with $n = 10$. **k**, Force–lifetime diagram of the catch–slip bond between $\alpha_5\beta_1$ integrin and FNIII$_{7-10}$, with or without treatments of antibody TS2/16 as indicated (from ref. 23). **l**, Response of subcellular CSK tension (left) and FA (right) rheostasis to TS2/16 treatment in human mesenchymal stem cells (HUMSCs) under 8% static equibiaxial stretch. Results were grouped into subsets on the basis of ground-state CSK tension values at $t = 0$ min (F_0). Whole-cell average response (black) was included to indicate changes in single-cell homeostasis. Data represent the mean ± s.e.m. with $n = 11$. In **g**–**i** and **l**, open red arrowheads indicated suppressed FA reinforcement in Phase I, and solid red arrowheads marked suppressed FA relaxation in Phase II. *P*-values were calculated using Student's paired sample *t*-test comparing data before ($t = 0$ min) and after ($t = 1$ or 30 min) stretch. NS, statistically not significant and $P > 0.05$.*, $P < 0.05$. Statistical analysis for different FA subsets is colour-coded as indicated.

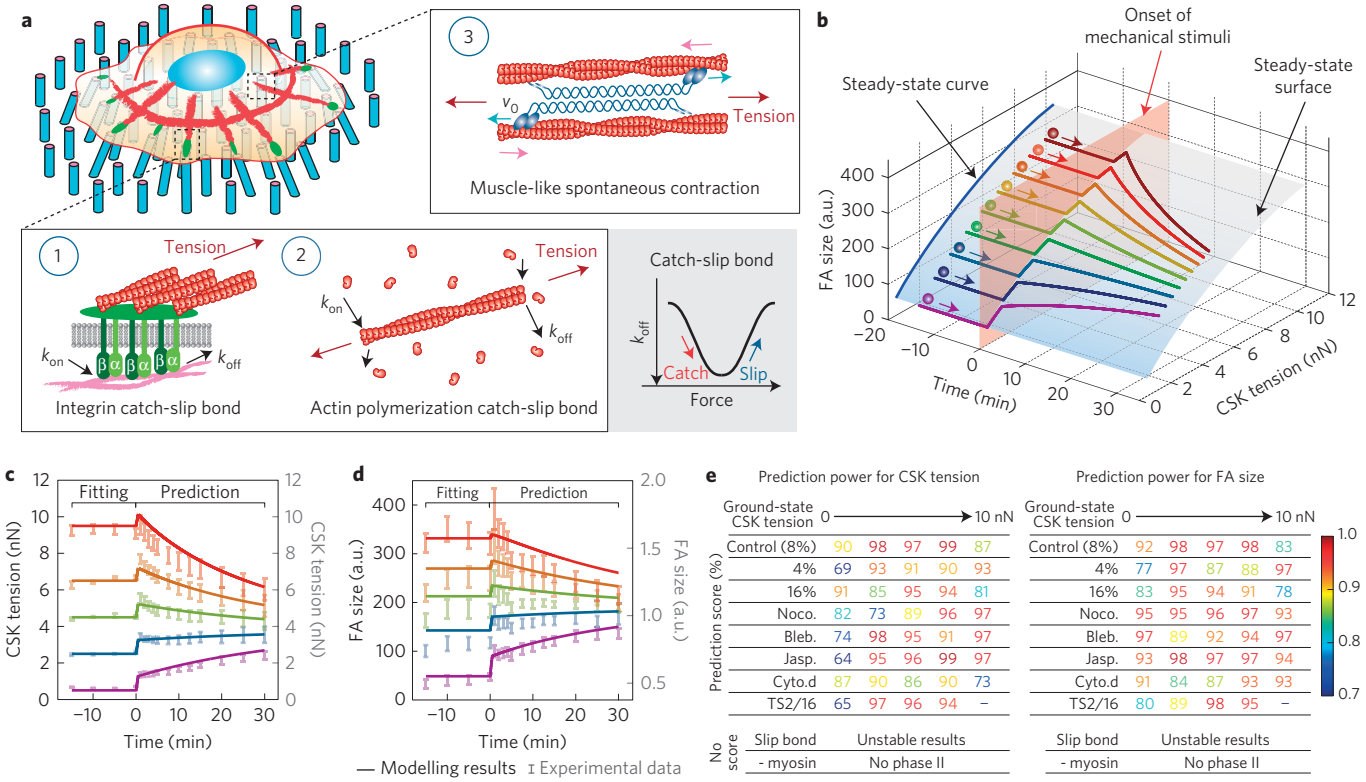

Figure 3 | Theoretical modelling of mechanosensitive subcellular rheostasis. a, Illustration of three key mechanisms incorporated in the theoretical framework, including catch–slip bonds in integrin and F-actin and muscle-like spontaneous contractility driven by myosin motor activity. **b**, Theoretical result showing a three-dimensional, stable solution surface (translucent blue) for temporal evolutions of CSK tension and FA size during single-cell homeostasis (see Biophysical Modeling in Supplementary Methods). Colour-coded trajectories simulated mechanosensitive rheostasis that depended on ground-state values of FA size and CSK tension. The onset of mechanical perturbation is indicated by a translucent pink surface. **c**,**d**, Theoretical results (solid curves) quantitatively agreed with experimental data (translucent error bars) for rheostatic behaviours of subcellular CSK tension (**c**) and FA size (**d**) in untreated REF-52 fibroblasts under 8% static equibiaxial stretch. Ground-state data obtained for $t \leq 0$ min were used for fitting model parameters, which were then employed to calculate rheostatic paths for $t > 0$ min. **e**, Predictive power of the theoretical model showing quantitative agreements between theoretical and experimental results on rheostatic responses of subcellular CSK tension and FA under different external perturbations or in the absence of certain key mechanisms in the model as indicated. In cases where subcellular rheostasis was experimentally observed, prediction scores, defined as one minus the average of absolute percentile error in the prediction segment for $t > 0$, were calculated. In theoretical calculations where the catch–slip bond or myosin motor activity was removed from the model, no prediction score was available owing to reasons as listed (see Supplementary Methods and Supplementary Fig. 18 for details).

We next investigated how heterogeneous, non-homeostatic responses of subcellular CSK tension and FA might collectively determine single-cell homeostasis. By grouping individual FAs on the basis of their corresponding ground-state CSK tension, our analysis revealed an expanded spectrum of graduated paths ('rheostasis') for both subcellular CSK tension and FA size that eventually converged onto their respective ground-state, whole-cell averages (Fig. 2a,b). Presenting subcellular variations during both Phase I ($t = 0$–1 min) and Phase II ($t = 1$–30 min) of the homeostasis in two-dimensional ground-state CSK tension–FA size diagrams further unravelled the dependence of subcellular rheostasis on ground-state values of CSK tension and FA size (Fig. 2c–f). Specifically, in Phase I, reinforcements of subcellular CSK tension and FA size appeared uniform across the cell, probably serving as a passive mechanical response to resist rapid cell deformation (Fig. 2c,e). In distinct contrast, in Phase II, dynamics of CSK tension and FA demonstrated a notable mechanosensitive transition. Subcellular CSK tension and FA with ground-state values greater than whole-cell averages underwent relaxation-like rheostasis; whereas those less than whole-cell averages experienced reinforcement-like rheostasis (Fig. 2d,f).

In addition to REF-52 fibroblasts, mechanosensitive subcellular rheostasis of CSK tension and FA was observed during single-cell mechanical homeostasis in human mesenchymal stem cells (HUMSCs) and human skin fibroblasts (HUSFs) when responding to 8% static equibiaxial stretch (Supplementary Fig. 6). Thus, rather than due to a self-similarity-like property governing mechanoresponsive behaviours across both cellular and subcellular scales, the apparent cellular-scale mechanical homeostasis was an emergent biological phenomenon driven by collective subcellular rheostasis of CSK tension and FA following distinct mechanosensitive compensatory patterns.

We further examined how mechanical stimulation severity affected single-cell homeostasis and subcellular rheostasis. Compared with 8% static equibiaxial stretch, 4% static stretch resulted in similar biphasic single-cell homeostasis and mechanosensitive subcellular rheostasis in REF-52 fibroblasts (Supplementary Fig. 7a–f). However, for REF-52 fibroblasts under 16% static equibiaxial stretch, a significant change in subcellular rheostasis was observed, where reinforcement of either CSK tension or FA with high ground-state values during Phase I was inhibited, leading to complete abrogation of biphasic dynamics of single-cell FA homeostasis (Supplementary Fig. 7g–l). 16% static equibiaxial stretch further compromised linear correlation between subcellular CSK tension and FA size in REF-52 fibroblasts (Supplementary Fig. 5g). Yet, strikingly, REF-52 fibroblasts under 16% static

equibiaxial stretch still retained single-cell mechanical homeostasis with temporal synchronization between subcellular CSK tension and FA size (Supplementary Fig. 5j and Supplementary Fig. 7g,h), suggesting single-cell homeostasis as a resilient property when responding to a broad range of external biophysical stimulation.

We next investigated how single-cell mechanical homeostasis might respond to perturbations to the CSK, which have been implicated in pathogenic contexts featuring dysregulation of mechanical homeostasis, such as cancer[2]. REF-52 fibroblasts were treated with small-molecule inhibitors targeting CSK integrity and tension: nocodazole, which depolymerizes microtubules and impedes FA disassembly[16]; blebbistatin, which inhibits myosin motor activity and thus CSK tension[17]; jasplakinolide, which enhances actin polymerization[18]; cytochalasin D, which blocks actin polymerization[19]. To minimize off-target effects, dosages of the inhibitors were optimized so that there was no significant change in cell area, FA size, CSK tension, or actin CSK architecture at ground states in inhibitor-treated cells (Supplementary Fig. 8). Of note, although the low dosage of cytochalasin D still appeared to affect the apparent cell phenotypes (Supplementary Fig. 8), it was required to elicit a significant change in single-cell homeostasis and thus to study corresponding variations in subcellular homeostasis (see discussions below).

Interestingly, on treatments with the inhibitors, single-cell homeostasis and subcellular rheostasis of CSK tension were maintained well in REF-52 fibroblasts under 8% static equibiaxial stretch (Fig. 2g–j, top panel and Supplementary Fig. 9a–e). However, significant variations in subcellular FA rheostasis were evident in inhibitor-treated cells. Specifically, nocodazole, blebbistatin and jasplakinolide treatments completely prevented FAs with high ground-state values from undergoing relaxation in Phase II (Fig. 2g–i, bottom panel and Supplementary Fig. 9f–i). Jasplakinolide treatment also abolished acute increase in FA size during Phase I (Fig. 2i, bottom panel and Supplementary Fig. 9i). These effects significantly biased subcellular FA rheostasis patterns and induced an effective exit of FA homeostasis at the single-cell level. Notably, although cytochalasin D did not significantly affect mechanosensitive rheostatic transition between reinforcement and relaxation, it largely abolished ground-state FAs sustaining high CSK tension and thus biased the proportions of distinct FA subsets participating in the rheostasis, leading to skewed FA homeostasis at single-cell level (Fig. 2j and Supplementary Fig. 9j). In addition, all inhibitor treatments reduced time-independent linear correlation, as well as temporal synchronization, between subcellular CSK tension and FA (Supplementary Fig. 10), consistent with the finding that FA but not CSK tension exhibited biased rheostasis under inhibitor treatments.

Given that force-dependent subcellular rheostatic patterns exhibited catch–slip-like behaviours, we further examined the regulatory role of catch–slip-like behaviours of the CSK–FA system in the maintenance of cellular homeostasis through subcellular rheostasis. Catch–slip bond mechanisms have been demonstrated as being critical to cellular mechanotransduction[20–26]. To examine specifically the role of integrin-mediated catch–slip bond in mechanosensitive subcellular rheostasis, HUMSCs were treated with an antibody (clone TS2/16) targeting human β_1 integrin before assayed with the SμPA for 8% static equibiaxial stretch. Antibody TS2/16 treatment shortens integrin–fibronectin bond lifetime under high forces and prolongs the lifetime at low forces[23] (Fig. 2k). Treatment with TS2/16 biased subcellular rheostasis and single-cell homeostasis of FA but not CSK tension (Fig. 2l), confirming FA dynamics as a more sensitive gating mechanism for cellular homeostasis compared to CSK tension. Specifically, TS2/16 treatment inhibited both the strengthening (Phase I) and relaxation (Phase II) phases for FAs with high ground-state values. Suppressed FA strengthening in Phase I was probably due to domination of the slip portion of integrin bond dynamics at high forces and a rapid switch from 'catch' to 'slip' mode after cell stretch. Subsequently suppressed relaxation (leading to an apparent stabilization phase) was probably attributable to prolonged integrin bond lifetime equivalent to a 're-catch' for a failing bond. These results provided convincing evidence supporting the involvement of integrin catch–slip-bond dynamics, and possibly other catch–slip bonds in the CSK–FA system, in mediating mechanosensitive FA rheostasis.

We next theorized mechanosensitive rheostasis using biophysical modelling. In light of our experimental findings, the model was comprised of three key mechanisms (Fig. 3a and Supplementary Figs 11 and 12 and Supplementary Methods): integrin catch–slip bonds, as required for FA rheostasis in Fig. 2l; F-actin catch–slip bonds[25], to mimic catch–slip-like behaviours in the CSK–FA system; and myosin motor activity[27], which drives muscle-like spontaneous contraction in response to external forces and was shown to be required for FA rheostasis in the inhibitor assays (Fig. 2h). Of note, the integrin and F-actin catch–slip bonds included in the biophysical mode could be readily generalized to incorporate other cellular machineries residing in the CSK–FA system that exhibit similar catch–slip behaviours, such as vinculin, filamin and α-actinin[21,22,26]. Dynamic remodelling of the actin CSK has been reported previously as a cellular response to external stretch[28,29]. However, there was no notable remodelling of actin stress fibres during subcellular rheostasis in response to 8% static equibiaxial stretch on the SμPA (Supplementary Fig. 13). Thus, remodelling of the actin CSK was not considered in the theoretical model.

The steady-state solution surface of CSK tension versus FA size generated from the biophysical model clearly illustrated their correlation at ground states as observed in the experiments (Fig. 3b and Supplementary Fig. 5). Simulation results also qualitatively recapitulated mechanosensitive rheostatic dynamics of both CSK tension and FA and its dependence on their respective ground-state values (Fig. 3b). Interestingly, by directly adapting data from previous experimental studies[23,25,30–33], as well as fitting model parameters using ground-state values ($t < 0$ min) of CSK tension and FA size (Supplementary Table 1), our model quantitatively predicted mechanosensitive rheostatic behaviours ($t > 0$ min) of CSK tension and FA in REF-52 fibroblasts in response to 8% cell stretch (Fig. 3c,d). By changing the stretch magnitude from 8% to 4% and 16%, respectively, while keeping all other model parameters unchanged, theoretical simulations further successfully recapitulated the subcellular rheostasis of CSK tension and FA under different cell stretch levels (Fig. 3e and Supplementary Fig. 14). Using ground-state data to fit and simulate effects of inhibitor treatments on different model parameters (Supplementary Table 1), we further achieved quantitative simulations of experimental results from inhibitor-treated cells (Fig. 3e and Supplementary Fig. 15a–d). Single-parameter studies using the biophysical model to mimic specific effects of individual inhibitors also supported the important roles of microtubule-mediated FA disassembly, myosin motor activity, and actin polymerization in selectively biasing mechanosensitive FA rheostasis (Supplementary Fig. 15e–h). Our modelling results also suggested that abolished reinforcement of FA size with high ground-state values in Phase I, as observed in REF-52 fibroblasts under 16% stretch or jasplakinolide treatment, was attributable to an instability-like phenomenon, where the steady-state solution curve describing stable states of CSK tension and FA was not available beyond a threshold (Supplementary Figs 14b,d and 15c,g, and 16).

Using modified integrin catch–slip-bond parameters on TS2/16 treatment (Supplementary Fig. 17a), the theoretical model successfully predicted a decrease and an increase in whole-cell average CSK tension and FA size, respectively, consistent with experimental results (Supplementary Fig. 17b–f). Importantly,

the model further recapitulated the effect of TS2/16 treatment in biasing subcellular FA rheostasis but not CSK tension, wherein only FAs with high ground-state CSK tension would demonstrate initial instability, followed by rapid re-stabilization to achieve an apparent suppressed rheostasis (Fig. 2l and Supplementary Fig. 17g,h).

To further examine whether the catch–slip-bond mechanism was indispensable for theoretical recapitulation of subcellular rheostasis, the integrin catch–slip bond in the model was replaced with a slip bond, resulting in a failure to recapitulate subcellular rheostasis due to instability of theoretical solutions after cell stretch (Supplementary Fig. 18a–c and Supplementary Methods). We further examined whether myosin motor activity was required for theoretical recapitulation of subcellular rheostasis by removing it from the model (Supplementary Methods). Interestingly, in the absence of myosin motor activity, the model could not simulate rheostatic dynamics in Phase II, even though Phase I reinforcement was still properly recapitulated by the model as the result of a passive mechanical response (Supplementary Fig. 18d–f).

Together, our theoretical studies clearly demonstrated the quantitative predictive power of the biophysical model and underscored the biophysical mechanisms underlying mechanosensitive subcellular rheostasis. The biophysical model, even though minimalistic and capable of being extended to incorporate additional subcellular components, was both sufficient and necessary for recapitulating the subcellular rheostasis of CSK tension and FA morphogenesis.

In conclusion, by using the SμPA cytometry in conjunction with live-cell imaging to map dynamic responses of subcellular CSK tension and FA with a one-to-one spatial registration, we demonstrated single-cell mechanical homeostasis as an emergent phenomenon driven by the mechanosensitive, collective subcellular rheostasis of CSK tension and FA. Importantly, biased rheostasis of FA, but not CSK tension, in response to perturbations on the CSK or integrin catch–slip-bond dynamics was shown to be gating the maintenance or exit of single-cell homeostasis. Our biophysical model provided a general framework to study the mechanosensitive rheostasis of CSK tension and FA and their diverse dynamics in response to different environmental and structural perturbations. Successful recapitulation of the rheostasis of CSK tension and FA using the biophysical model underscored the critical roles of force-sensitive molecular machineries, including integrin and F-actin catch–slip bonds and myosin motor activity, in regulating mechanical homeostasis through physical emergence. Together, our results on both experimental and theoretical fronts provide quantitative insights regarding the physical origin of single-cell mechanical homeostasis and its regulation through complex, collective subcellular rheostasis.

Methods

Methods and any associated references are available in the online version of the paper.

Received 3 January 2015; accepted 4 May 2016; published online 30 May 2016

References

1. Wang, N. *et al*. Cell prestress. I. Stiffness and prestress are closely associated in adherent contractile cells. *Am. J. Physiol. Cell Physiol.* **282,** C606–C616 (2002).
2. Paszek, M. J. *et al*. Tensional homeostasis and the malignant phenotype. *Cancer Cell* **8,** 241–254 (2005).
3. Solon, J., Levental, I., Sengupta, K., Georges, P. C. & Janmey, P. A. Fibroblast adaptation and stiffness matching to soft elastic substrates. *Biophys. J.* **93,** 4453–4461 (2007).
4. Rape, A. D., Guo, W.-H. & Wang, Y.-L. The regulation of traction force in relation to cell shape and focal adhesions. *Biomaterials* **32,** 2043–2051 (2011).
5. Webster, K. D., Ng, W. P. & Fletcher, D. A. Tensional homeostasis in single fibroblasts. *Biophys. J.* **107,** 146–155 (2014).
6. Schwartz, M. W. *et al*. Cooperation between brain and islet in glucose homeostasis and diabetes. *Nature* **503,** 59–66 (2013).
7. Ritsma, L. *et al*. Intestinal crypt homeostasis revealed at single-stem-cell level by *in vivo* live imaging. *Nature* **507,** 362–365 (2014).
8. Maloy, K. J. & Powrie, F. Intestinal homeostasis and its breakdown in inflammatory bowel disease. *Nature* **474,** 298–306 (2011).
9. Vermeulen, L. & Snippert, H. J. Stem cell dynamics in homeostasis and cancer of the intestine. *Nature Rev. Cancer* **14,** 468–480 (2014).
10. Chen, C. S. Mechanotransduction—a field pulling together? *J. Cell Sci.* **121,** 3285–3292 (2008).
11. Vogel, V. & Sheetz, M. Local force and geometry sensing regulate cell functions. *Nature Rev. Mol. Cell Biol.* **7,** 265–275 (2006).
12. Deakin, N. O. & Turner, C. E. Paxillin comes of age. *J. Cell Sci.* **121,** 2435–2444 (2008).
13. Galbraith, C. G., Yamada, K. M. & Sheetz, M. P. The relationship between force and focal complex development. *J. Cell Biol.* **159,** 695–705 (2002).
14. Oakes, P. W., Beckham, Y., Stricker, J. & Gardel, M. L. Tension is required but not sufficient for focal adhesion maturation without a stress fiber template. *J. Cell Biol.* **196,** 363–374 (2012).
15. Chen, Y., Pasapera, A. M., Koretsky, A. P. & Waterman, C. M. Orientation-specific responses to sustained uniaxial stretching in focal adhesion growth and turnover. *Proc. Natl Acad. Sci. USA* **110,** E2352–E2361 (2013).
16. Ezratty, E. J., Partridge, M. A. & Gundersen, G. G. Microtubule-induced focal adhesion disassembly is mediated by dynamin and focal adhesion kinase. *Nature Cell Biol.* **7,** 581–590 (2005).
17. Allingham, J. S., Smith, R. & Rayment, I. The structural basis of blebbistatin inhibition and specificity for myosin II. *Nature Struct. Mol. Biol.* **12,** 378–379 (2005).
18. Holzinger, A. Jasplakinolide: an actin-specific reagent that promotes actin polymerization. *Methods Mol. Biol.* **586,** 71–87 (2009).
19. Flanagan, M. D. & Lin, S. Cytochalasins block actin filament elongation by binding to high affinity sites associated with F-actin. *J. Biol. Chem.* **255,** 835–838 (1980).
20. Guo, B. & Guilford, W. H. Mechanics of actomyosin bonds in different nucleotide states are tuned to muscle contraction. *Proc. Natl Acad. Sci. USA* **103,** 9844–9849 (2006).
21. Ferrer, J. M. *et al*. Measuring molecular rupture forces between single actin filaments and actin-binding proteins. *Proc. Natl Acad. Sci. USA* **105,** 9221–9226 (2008).
22. del Rio, A. *et al*. Stretching single talin rod molecules activates vinculin binding. *Science* **323,** 638–641 (2009).
23. Kong, F., García, A. J., Mould, A. P., Humphries, M. J. & Zhu, C. Demonstration of catch bonds between an integrin and its ligand. *J. Cell Biol.* **185,** 1275–1284 (2009).
24. Luo, T. *et al*. Understanding the cooperative interaction between myosin II and actin cross-linkers mediated by actin filaments during mechanosensation. *Biophys. J.* **102,** 238–247 (2012).
25. Lee, C.-Y. *et al*. Actin depolymerization under force is governed by lysine 113:glutamic acid 195-mediated catch-slip bonds. *Proc. Natl Acad. Sci. USA* **110,** 5022–5027 (2013).
26. Luo, T., Mohan, K., Iglesias, P. A. & Robinson, D. N. Molecular mechanisms of cellular mechanosensing. *Nature Mater.* **12,** 1064–1071 (2013).
27. Mitrossilis, D. *et al*. Single-cell response to stiffness exhibits muscle-like behavior. *Proc. Natl Acad. Sci. USA* **106,** 18243–18248 (2009).
28. Chen, C. *et al*. Fluidization and resolidification of the human bladder smooth muscle cell in response to transient stretch. *PLoS ONE* **5,** e12035 (2010).
29. Tondon, A., Hsu, H.-J. & Kaunas, R. Dependence of cyclic stretch-induced stress fiber reorientation on stretch waveform. *J. Biomech.* **45,** 728–735 (2012).
30. Finer, J. T., Simmons, R. M. & Spudich, J. A. Single myosin molecule mechanics: piconewton forces and nanometre steps. *Nature* **368,** 113–119 (1994).
31. Veigel, C., Molloy, J. E., Schmitz, S. & Kendrick-Jones, J. Load-dependent kinetics of force production by smooth muscle myosin measured with optical tweezers. *Nature Cell Biol.* **5,** 980–986 (2003).
32. Kumar, S. *et al*. Viscoelastic retraction of single living stress fibers and its impact on cell shape, cytoskeletal organization, and extracellular matrix mechanics. *Biophys. J.* **90,** 3762–3773 (2006).
33. Lu, L., Oswald, S. J., Ngu, H. & Yin, F. C. P. Mechanical properties of actin stress fibers in living cells. *Biophys. J.* **95,** 6060–6071 (2008).

Acknowledgements

We thank A. Bershadsky for providing REF-52 cells, G. J. Fisher for providing human skin fibroblasts, and A. Liu for comments on the manuscript. This work is supported by the National Science Foundation (CMMI 1129611 and CBET 1149401), the National Institutes of Health (R21 HL114011 and R21 EB017078), the American Heart Association (12SDG12180025), and the Department of Mechanical Engineering at the University of Michigan, Ann Arbor. The Lurie Nanofabrication Facility at the University of Michigan,

a member of the National Nanotechnology Infrastructure Network (NNIN) funded by the National Science Foundation, is acknowledged for support in microfabrication.

Author contributions

S.W. and J.F. designed experiments; S.W., Y.S. and W.C. performed experiments and modelling; S.W., Y.S. and J.F. analysed data and wrote the manuscript; J.F. supervised the project. All authors edited and approved the final manuscript.

Additional information

Supplementary information is available in the online version of the paper. Reprints and permissions information is available online at www.nature.com/reprints. Correspondence and requests for materials should be addressed to J.F.

Competing financial interests

The authors declare no competing financial interests.

Methods

Fabrication and functionalization of stretchable micropost array. Stretchable micropost array (SμPA) was fabricated with conventional semiconductor microfabrication and soft lithography before functionalization using micro-contact printing[34]. The entire fabrication process consisted of four steps: fabrication of a Si micropost mould, fabrication of a poly-dimethylsiloxane (PDMS; Sylgard 184, Dow-Corning) micropost array, functionalization of the PDMS micropost array, and integration of the PDMS micropost array onto a stretchable PDMS basal membrane.

Fabrication of Si micropost mould. Conventional high-resolution photolithography and deep reactive-ion etching (DRIE) techniques were used for the fabrication of the Si micropost mould. A 5× reduction step-and-repeat projection stepper (Nikon NSR2005i9, Nikon Precision) was used for photoresist patterning. DRIE was performed with an inductively coupled plasma deep reactive-ion etcher (ICP Deep Trench Etching Systems, Surface Technology Systems). The height of the Si micropost was controlled by varying the etching time during DRIE. After stripping photoresist with Piranha solution (4:1 v/v H_2SO_4/H_2O_2), the dimensions of the Si micropost were measured using surface profilometry (Prometrix P-10, KLA-Tenco) and scanning electron microscopy (SEM; JEOL6320FV, JEOL USA). The Si mould was passivated with trichloro (1H, 1H, 2H, 2H-perfluorooctyl) silane (Sigma-Aldrich) for 4 h under vacuum to aid subsequent release of negative PDMS templates from the Si mould. The Si mould used in this work contained hexagonally spaced posts with a post diameter of 1.83 μm, a post height of 8.3 μm, and a post centre-to-centre distance of 4 μm. Finite element modelling for mechanical characterization revealed that PDMS microposts replica moulded from the Si mould had a nominal spring constant (K_{post}) of 7.2 nN μm^{-1}.

Fabrication of PDMS micropost array. The PDMS micropost array was generated by replica moulding as previously described[35–38]. Briefly, to make a negative template containing an array of holes, PDMS prepolymer with a 10:1 base to curing agent ratio was poured over the Si micropost mould and cured at 110 °C for 20 min. The negative PDMS mould was peeled off from the Si micropost mould before being oxidized with air plasma (Plasma Prep II, SPI Supplies) and passivated with trichloro (1H, 1H, 2H, 2H-perfluorooctyl) silane vapour overnight under vacuum. In parallel, a coverslip was passivated with trichloro (1H, 1H, 2H, 2H-perfluorooctyl) silane vapour overnight under vacuum before being spin-coated with a thin layer of PDMS prepolymer at 2,000 r.p.m. for 30 s (Laurell Technologies). PDMS on the coverslip was cured at 110 °C for 20 min to form a releasable thin PDMS layer. The final PDMS micropost array was generated by pouring PDMS prepolymer over the PDMS negative template, degassing under vacuum, flipping and placing the PDMS-coated coverslip in direct contact with the negative PDMS template, curing at 110 °C for 40 h, and peeling off the PDMS micropost array from the negative PDMS template. When peeling induced the collapse of PDMS microposts, we recovered PDMS microposts by sonication in 100% ethanol for 30 s followed by dry-release with liquid CO_2 using a critical point dryer (Samdri-PVT-3D, Tousimis).

Functionalization of PDMS micropost array. Functionalization of the PDMS micropost array was achieved using micro-contact printing[37,38]. Briefly, flat, featureless PDMS stamps were generated and immersed in a solution containing both fibronectin (50 μg ml^{-1}; Sigma-Aldrich) and Alexa-Fluor 647-conjugated fibrinogen (25 μg ml^{-1}; Invitrogen) for 1 h. PDMS stamps were rinsed with deionized (DI) water before being blown dry using nitrogen gas. Protein-coated PDMS stamps were then placed in conformal contact with the PDMS micropost array pre-treated with ultraviolet/ozone (UVO-CLEANER, Jelight) to transfer adhesive proteins from stamps to the tops of the PDMS microposts.

Integration of PDMS micropost array onto a stretchable PDMS basal membrane. To generate a PDMS basal membrane, PDMS prepolymer was spin-coated onto 100 mm Petri dish covers at 500 r.p.m. for 30 s, followed by curing at 70 °C for 40 h. The resultant PDMS basal membrane had a thickness of 200–300 μm. In parallel, the thin PDMS layer holding the PDMS micropost array was gently peeled off from the coverslip, flipped, and brought into conformal contact with a PDMS pad before the backside of the PDMS layer was treated with air plasma. The thin PDMS layer holding the PDMS micropost array was then bonded to the PDMS basal membrane through plasma-assisted PDMS–PDMS bonding to generate the final SμPA. The SμPA was submerged sequentially in 100% ethanol (10 s), 70% ethanol (10 s), 30% ethanol (10 s), DI water (10 s), and 0.2% w/v Pluronics F-127 solution (Sigma-Aldrich; 1 h), before being rinsed three times with DI water. Functionalized SμPA could be stored in phosphate-buffered saline (PBS; Invitrogen) solution for up to one week before use.

Cell culture and reagents. Both rat embryo fibroblast cell line REF-52 stably expressing yellow fluorescent protein (YFP)–paxillin fusion protein (gift from A. D. Bershadsky, Mechanobiology Institute at the National University of Singapore and the Weizmann Institute of Science; ref. 39) and human skin fibroblasts (HUSFs; gift from G. J. Fisher, the University of Michigan, Ann Arbor; ref. 40) were maintained in high-glucose Dulbecco's modified Eagle's medium (DMEM; Invitrogen) supplemented with 10% fetal bovine serum (FBS; Invitrogen), 4 mM L-glutamine (Invitrogen), 100 units ml^{-1} penicillin (Invitrogen), and 100 μg ml^{-1} streptomycin (Invitrogen) at 37 °C and 5% CO_2. Human mesenchymal stem cells (HUMSCs; Lonza) were maintained in MesenPRO RS medium (Invitrogen) at 37 °C and 5% CO_2. LentiBrite paxillin–green fluorescent protein (GFP) lentiviral biosensors (Millipore) were transduced into HUSFs and HUMSCs at multiplicity of infection (MOI) of 50–80 according to manufacturer's protocol. CellLight actin-RFP construct (Invitrogen) was transfected into REF-52 fibroblast cells at particles per cell (PPC) of 60 according to manufacturer's protocol. HUMSCs were authenticated by Lonza using immunostaining, characteristic cell morphology, and flow cytometry. REF-52 fibroblasts and HUSFs were identified by characteristic cell morphology and cell surface markers. All cell lines were tested for mycoplasma contamination using the LookOut Mycoplasma PCR Detection Kit from Sigma-Aldrich.

When cells became 90% confluent, cells were washed twice with PBS and incubated with 0.25% trypsin–EDTA buffer solution (Invitrogen) for 2 min for cell re-suspension. Single REF-52 fibroblasts, HUSFs and HUMSCs were seeded at a density of 8,000 cells cm^{-2}, 4,000 cells cm^{-2} and 2,000 cells cm^{-2}, respectively, on the SμPA and were allowed to spread out for at least 6 h before cell stretch assays (Supplementary Fig. 1a,b). To reduce background fluorescence, phenol red-free growth medium (Invitrogen) was used during live-cell fluorescence imaging.

To perturb the actin cytoskeleton (CSK) in REF-52 fibroblasts, small-molecule inhibitors targeting the CSK integrity and tension, including 50 nM nocodazole (Sigma-Aldrich), which depolymerizes microtubules and impedes FA disassembly[16]; 10 μM blebbistatin (Cayman Chemical), which inhibits myosin motor activity and thus CSK tension[17]; 10 nM jasplakinolide (Cayman Chemical), which enhances actin polymerization[18]; and 200 nM cytochalasin D (Tocris bioscience), which blocks actin polymerization[19], were supplemented to cell growth medium for 2 h before cell stretch assays. Dosages of the inhibitors were optimized by titration to minimize their off-target effects on cell area, focal adhesion (FA) size, CSK tension, and actin CSK architecture (Supplementary Fig. 8). Of note, although the low dosage of cytochalasin D applied in this study still appeared to affect cell mechanobiological states (phenotypes), significant portions of FAs, the actin CSK, and CSK tension still remained to support our investigations of the roles of the CSK integrity and tension on single-cell mechanical homeostasis and subcellular rheostasis.

To modulate the catch–slip bond property of integrin–fibronectin bond for HUMSCs, anti-human integrin $\beta 1$ antibody TS2/16 (Santa Cruz) was added to cell growth medium at 5 μg ml^{-1} for 2 h before cell stretch assays.

Cell stretch assay. A custom-made, vacuum-driven cell stretching device (CSD) was developed to stretch the SμPA (Supplementary Fig. 1c,d)[34]. The CSD contained a circular viewing aperture surrounded by a vacuum chamber (Supplementary Fig. 1c). For cell stretch assays, cells were first seeded onto the SμPA and cultured for at least 6 h, before the SμPA was inverted and mounted onto the CSD and submerged in pre-warmed culture medium inside a glass-bottom dish to facilitate high-resolution live-cell imaging. The PDMS micropost array on the SμPA was centred on the viewing aperture of the CSD to permit direct visualization of microposts under microscopy. The CSD was connected to a portable vacuum generator (Vacu-Cell Vacuum System, C&L Instruments) and a vacuum regulator (Airtrol) to control the onset and magnitude of vacuum. The CSD was activated for cell stretch by applying a vacuum to draw the periphery of the PDMS basal membrane into the vacuum chamber, causing the central area of the SμPA holding the PDMS micropost array to stretch equibiaxially (Supplementary Fig. 1c). The stretch magnitude of the SμPA was determined by means of regularly positioned PDMS microposts as fiduciary markers.

During cell stretch assays, each single cell was continuously monitored for 15 min before cell stretch (Supplementary Fig. 1e). At the onset of stretch, a rapid 4%, 8%, or 16% step increase of cell stretch was applied and was held constant for another 30 min (Supplementary Fig. 1e).

Fluorescence imaging. Live-cell fluorescence imaging was performed using a monochrome charge-coupled device (CCD) camera (AxioCam, Carl Zeiss MicroImaging) attached to an inverted epi-fluorescence microscope (Zeiss Axio Observer Z1, Carl Zeiss Microimaging) enclosed in an environmental incubator (XL S1 incubator, Carl Zeiss MicroImaging) maintaining cell culture at 37 °C and 5% CO_2. Images of micropost tops, FAs containing fluorescent protein (FP)–paxillin fusion proteins, and/or RFP-fused actin were recorded using a 40× EC Plan-Neofluar objective (NA 0.75, Ph2, Carl Zeiss MicroImaging) (Supplementary Fig. 1a,b). On stretch, the basal PDMS membrane of the SμPA inevitably generated vertical deformation, causing out-of-focus movements of cells cultured on the microposts, which was corrected manually by re-adjusting the focal plane within 10 s after the onset of stretch.

Quantitative analysis of cytoskeleton tension and focal adhesion. Quantitative analysis of subcellular CSK tension was performed using a custom-developed MATLAB program (Mathworks) (Supplementary Fig. 2a)[38]. Briefly, individual micropost tops were determined by two-dimensional (2D) Gaussian fitting, where 'windows' were drawn enclosing single posts and were adjusted to centre the post tops. Post centroids calculated from the previous step were then refined by applying 2D Gaussian fitting again. Undeflected microposts without cell attachment were manually selected as reference posts to generate an ideal array of force-free microposts. Using undeflected 'free' posts as references, deflections of microposts underneath a cell were quantified and converted to horizontal traction forces (CSK tension) by multiplying post deflection with the nominal post spring constant K_{post}.

The dynamics of FA was examined by continuously monitoring clustering of FP–paxillin on micropost tops (Supplementary Fig. 2b–g). During image processing, background fluorescence was first determined through performing morphological opening with a disk structure element of the same diameter as the PDMS micropost. Subtraction of background fluorescence was then conducted to deterrmine the FP–paxillin intensity in individual FAs localized on PDMS micropost tops. To spatially register each single FA to CSK tension, the fluorescent image of PDMS micropost tops was converted to a binary image serving as a mask to detect individual FAs confined on micropost tops. It should be noted that individual circles in the FA detection mask were enlarged to 1.5 times the original post size to ensure full enclosure and thus accurate measurements of FAs. Total fluorescence intensity of FP–paxillin confined on individual micropost tops was quantified as the FP–paxillin intensity per FA, or simply FA size.

Compensation of fluorescence quenching. Calibration curves for different fluorescent proteins and cell stretch levels were obtained to compensate fluorescence quenching due to photobleaching and light path variation caused by cell stretch (Supplementary Fig. 3a,b). Briefly, cells seeded on the SμPA were washed twice with PBS before being fixed with 4% paraformaldehyde (PFA; Electron Microscopy Sciences) in a CSK buffer (10 mM PIPES, 100 mM sodium chloride, 300 mM sucrose, 3 mM magnesium chloride, and pH adjusted to 6.9; Sigma-Aldrich) for 30 min. Cells were then washed twice with PBS before permeabilization with 0.1% Triton X-100 (Sigma-Aldrich) for 10 min. Cell stretch assays were conducted on fixed cells to obtain the total FP–paxillin intensity in each single cell as a function of time, using the same data acquisition frequency (sampling rate) as used in live-cell experiments. Two exponential functions were then used for best fitting of the decay of total FP–paxillin intensity in single cells before and after the onset of cell stretch, respectively (Supplementary Fig. 3c). These exponential functions were used as calibration curves for compensating fluorescence quenching in live-cell assays.

Scanning electron microscopy sample preparation. For scanning electron microscopy (SEM) of cell samples, cells were washed three times with 50 mM Na-cacodylate buffer (pH 7.3; Sigma-Aldrich), fixed for 1 h with 2% glutaraldehyde (Electron Microscopy Science) in 50 mM Na-cacodylate buffer, and dehydrated in a graded series of ethanol concentrations through 100% over a period of 1.5 h. Dehydration in 100% ethanol was performed three times. After washing with 100% ethanol, dehydrated samples were dried with liquid CO_2 using a critical point dryer. Samples were mounted on stubs and sputter-coated with gold palladium before being observed and photographed in SEM (Hitachi SU8000 ultrahigh-resolution microscope; Hitachi High Technologies America).

Cross-correlation analysis between cytoskeleton tension and focal adhesion. Dynamic synchronization between subcellular FAs and their associated CSK tension was evaluated using cross-correlation analysis[41]. Linear interpolation was first conducted to achieve a constant sampling frequency for FA size and CSK tension data sets while increasing the sampling resolution to 0.1 min. Refined data sets of CSK tension and FA size were denoted as A and B, respectively, with indices from 1 to N corresponding to the time t from −15 min to 30 min with an interval of 0.1 min. Because FA size B was relatively stable at both the beginning and the end of cell stretch assays, the FA size data set B was extended below $t=-15$ min and beyond $t=30$ min using its steady-state values at $t=-15$ and 30 min, respectively, for cross-correlation analysis. Specifically, for the extended FA size data set B_e, $B_e(1)=B_e(2)=\cdots=B_e(N-1)=B_e(N)=B(1), B_e(N+1)=B(1), B_e(N+2)=B(2), \cdots, B_e(2N-1)=B(N-1), B_e(2N)=B(N)$, and $B_e(2N+1)=B_e(2N+2)=\cdots=B_e(3N-1)=B_e(3N)=B(N)$, wherein $B(1)$ and $B(N)$ were the steady-state FA values at $t=-15$ and 30 min, respectively. Discrete cross-correlation CC(i) and discrete normalized cross-correlation NCC(i) between the CSK tension data set A and the FA size data set B were calculated as $CC(i)=\sum_{k=1}^{N} A(k)\cdot B_e(i+k-1)$ and $NCC(i)=CC(i)/\sqrt{\sum_{k=1}^{N} A^2(k)\cdot\sum_{k=1}^{N} B_e^2(i+k-1)}$, respectively, where index i ranged from 1 to $2N+1$, corresponding to the time axis t from −45 min to 45 min with an interval of 0.1 min. Discrete cross-correlation CC(i) and discrete normalized cross-correlation NCC(i) were further converted to CC(t) and NCC(t), respectively, where the greatest value of NCC(t) determined the maximum normalized cross-correlation between CSK tension A and FA size B. The time point at which NCC(t) reached its maximum determined the time delay of FA size B relative to CSK tension A and was designated in this work as the 'CSK tension—FA size cross-correlation time delay'.

Biophysical modelling. The biophysical model characterizing the dynamics of subcellular CSK tension and FA on cell stretch was comprised of three key mechanisms: integrin catch–slip bonds[23], which were shown in this work as being required for FA rheostasis (Fig. 2l); F-actin catch–slip bonds[25], to recapitulate catch–slip-like behaviours in the FA–CSK mechanical network; and myosin motor activity[27], which drives muscle-like spontaneous contraction in response to external forces and was shown as being required for FA rheostasis (Fig. 2h). Detailed biophysical modelling can be found in Supplementary Methods.

Code availability. Theoretical modelling was computed using MatLab with a custom-written code, which is available upon request.

References

34. Mann, J. M., Lam, R. H. W., Weng, S., Sun, Y. & Fu, J. A silicone-based stretchable micropost array membrane for monitoring live-cell subcellular cytoskeletal response. *Lab Chip* **12,** 731–740 (2012).
35. du Roure, O. Force mapping in epithelial cell migration. *Proc. Natl Acad. Sci. USA* **102,** 2390–2395 (2005).
36. Saez, A., Buguin, A., Silberzan, P. & Ladoux, B. Is the mechanical activity of epithelial cells controlled by deformations or forces? *Biophys. J.* **89,** L52–L54 (2005).
37. Fu, J. *et al*. Mechanical regulation of cell function using geometrically modulated elastomeric substrates. *Nature Methods* **7,** 733–736 (2010).
38. Yang, M. T., Fu, J., Wang, Y.-K., Desai, R. A. & Chen, C. S. Assaying stem cell mechanobiology on microfabricated elastomeric substrates with geometrically modulated rigidity. *Nature Protoc.* **6,** 187–213 (2011).
39. Alexandrova, A. Y. *et al*. Comparative dynamics of retrograde actin flow and focal adhesions: formation of nascent adhesions triggers transition from fast to slow flow. *PLoS ONE* **3,** e3234 (2008).
40. Li, Y. *et al*. Age-associated increase of skin fibroblast-derived prostaglandin E2 contributes to reduced collagen levels in elderly human skin. *J. Invest. Dermatol.* **135,** 2181–2188 (2015).
41. Lu, S. *et al*. Decipher the dynamic coordination between enzymatic activity and structural modulation at focal adhesions in living cells. *Sci. Rep.* **4,** 5756 (2014).